Quantitative imaging of ^{226}Ra ultratrace distribution using digital autoradiography: Case of doped celestines

Sophie Billon, Paul Sardini, Axel Angileri, Catherine Beaucaire, Jean Claude Parneix, Marja Siitari-Kauppi, Michael Descostes

Quantitative imaging of ^{226}Ra ultratrace distribution using digital autoradiography: case of doped celestines.

Sophie Billon[(1)], Paul Sardini[(2)], Axel Angileri[(2)], Catherine Beaucaire[(3)], Jean Claude Parneix[(1)], Marja Siitari-Kauppi[(4)], Michael Descostes[(5)]

[(1)] *ERM company, 4 rue Carol Heitz 86000 Poitiers, France*

[(2)] *Université de Poitiers, UMR 7285, IC2MP, rue Michel Brunet, Bat. 35, 86073 Poitiers cedex 9, France*

[(3)] *DEN-Service d'Etude du Comportement des Radionucléides (SECR), CEA, Université Paris-Saclay, F-91191 Gif-sur-Yvette, France*

[(4)] *University of Helsinki, Department of Chemistry, P.O. Box 55, 00014 University of Helsinki, Finland*

[(5)] *ORANO Mining- R&D Dpt, Tour AREVA, 1 Place Jean Millier, 92084 Paris La Défense, France*

Corresponding Author : *Sophie Billon*

sophie.billon@erm-poitiers.fr

ERM company, 4 rue Carol Heitz 86000 Poitiers, France

Abstract

The ability of the autoradiographic device BeaQuant™ is evaluated herein to quantitatively map the ultratrace element ^{226}Ra distributed spatially in celestine ($SrSO_4$) grains/crystals. ^{226}Ra doped celestines have been obtained from coprecipitation and recrystallization experiments, and have been characterized with high purity germanium gamma detector (HPGe), giving specific activities ranging from 3251 to 32523 $Bq.g^{-1}$. Alpha autoradiographs of polished sections from doped celestines have been obtained using BeaQuant™. These alpha maps have been compared to the celestine grains/crystals arrangement observed with a scanning electron microscope (SEM). At the sample scale, celestine grains are responsible of an alpha signal, indicating that ^{226}Ra is detectable in celestine from its alpha emissions. ^{226}Ra distribution has also been investigated at the celestine grains/crystals scale: the crystal/grain properties do not allow to decide if the distribution process is homogeneous or not, i.e. if there is a chemical zoning into the crystal/grain. The counting of alpha particles by autoradiography has been

compared with the total activity of the ^{226}Ra doped celestines by gamma counting (HPGe technique). This comparison was performed by standardizing the measured activities to the same celestine volume, which has been determined by performing a threshold on SEM grey level images to assess to the celestine surface and using Geant4 Monte Carlo simulation toolkit to assess to the emission depth of the particles in celestine. A very good linear correlation between gamma activity and alpha counting from autoradiographs is obtained for all the samples, demonstrating the ability of BeaQuant™ to quantify ^{226}Ra in any points of the millimetric section samples, at a resolution of 20 µm.

Keywords : Celestine; ^{226}Ra; alpha counting/mapping; autoradiography; Geant4; partition coefficient.

1. Introduction

The present work aims to locate the fifth descendant of the ^{238}U decay series, the ^{226}Ra, which is an alpha emitter. After uranium ore processing, mill tailings still present radioactivity due to remaining U, but more specifically to all other radioactive members of the ^{238}U decay chain, such as ^{226}Ra (Déjeant et al., 2014, 2016). Surface disposal, which is the most common storage of uranium mill tailings, exposes a large surface area to the interactions with surface water systems, increasing the risk of radionuclides release. From an environmental point of view, ^{226}Ra raises problems due to 1) its mobility (Phrommavanh et al., 2013; Sajih et al., 2014; Leermakers et al., 2016; Reinoso-Maset and Ly, 2016; Robin et al., 2017; Bordelet et al., 2018; Lestini et al., 2019), 2) its long half-life ($T_{1/2}$ = 1600 y), and 3) the fact it controls the radioactive emissions of half of the ^{238}U decay series (after ^{226}Ra, the radionuclides of ^{238}U decay series have short half-life). Moreover, as all daughters of the ^{238}U, very low ^{226}Ra content is responsible of high activity. Considering the ^{238}U decay chain at secular equilibrium, ^{226}Ra content is nearly 3 $\times 10^{+6}$ lower than ^{238}U content. In other words, if ^{238}U is present at a concentration of 80 ppm (corresponding to a specific ^{238}U activity of 1 Bq.g^{-1} ore) in an ore at secular equilibrium, the content of ^{226}Ra is about 27 ppt (corresponding to a specific ^{226}Ra activity of 1 Bq.g^{-1} ore).

To study the ^{226}Ra properties (mobility, migration, sorption) into a given geological system, it is needed to locate accurately the radionuclide in the samples. ^{226}Ra mobility is mainly controlled by surface interactions onto minerals (carbonates, clay minerals, metal oxides),

however it can also be incorporated in sulfates crystal lattice such as barite ($BaSO_4$) and celestine ($SrSO_4$), through solid-solution processes (Zhang et al., 2014; Lestini et al., 2019). After identifying the phase acting as a trap for ^{226}Ra, it could then be possible to study its retention mechanism, its retention potential expressed with a partition coefficient K_d, as well as its long-term sustainability that are key points to develop plan tailings management.

Until now, identification of ^{226}Ra bearing minerals is mainly investigated with the technique of chemical sequential leaching coupled to alpha spectrometry (Blanco et al., 2004; Menozzi et al., 2016). This technique is however a bulk method and tedious. It is difficult to control the chemical processes during leaching steps, in addition it is a destructive and a time-consuming method (Bacon and Davidson, 2008). More recently, Kalnins et al. (2019) proved the ability of an autoradiographic emulsion to map alpha tracks in natural occurring uranium-bearing minerals (uraninite) with low radionuclide concentrations, with a resolution close to the micrometer. The alpha tracks counting provided also a quantitative information, which has been checked with ZnS alpha counter.

A promising new technology, the digital autoradiography using BeaQuant™ radioimager, is investigated in the present work, to both quantify and locate the problematic ultratrace radioelement ^{226}Ra (Donnard et al., 2009, Sardini et al, 2016). BeaQuant™ uses a micro-pattern gaseous detector (MPGD), which can detect and map separately alpha and beta emissions. The detection efficiency is better for alpha particles due to their short ranges in gas and their high energies of emission able to strongly ionize the gas particles (Billon et al., 2019a). Thanks to these features and furthermore because ^{226}Ra is an alpha emitter, the detection and location of ^{226}Ra is performed with BeaQuant™ using the alpha emissions of the ^{226}Ra decay chain. Angileri et al. (2018) have compared the theorical alpha activity of uranium minerals (uraninite and uranophane) included into geomaterials, to the alpha counting with BeaQuant™. The theoretical alpha activity, deduced from the uranium content (wt% of U) measured with microprobe, was similar to the BeaQuant™ measurement, demonstrated the quantitative nature of BeaQuant™. Since alpha counting from BeaQuant™ is quantitative for ^{238}U decay chain nuclides, it can be assumed to be a qualified method if only a part of the chain is considered, i.e. ^{226}Ra and its descendants. The paper aims to determine the quantitative mapping of ^{226}Ra with digital autoradiography in minerals.

Sulfates are minerals of interest because they are ubiquitous in tailings, due to the use of sulfuric acid for ore processing. Celestine ($SrSO_4$), which forms solid solution with ^{226}Ra, has been used in the present work. ^{226}Ra doped-celestine crystals have been obtained from two coprecipitation

experiments (samples S1 and S2) and natural celestine grains (sample S3) have been subjected to recrystallization experiment in a ^{226}Ra spiked solution.

Scanning Electron Microscope (SEM) observations have been performed to study the celestine crystals/grains arrangement in the samples (i.e. crystals/grains dispersed into resin) for comparison to the ^{226}Ra autoradiography mapping obtained with BeaQuant™ (^{226}Ra location on the sample scale). ^{226}Ra distribution in celestine crystals/grains has also been studied by comparing crystals/grains geometry to BeaQuant™ alpha counting (^{226}Ra distribution on the crystal/grain scale). The distribution process is of great interest to understand solid-solution phenomenon which is theoretically described with the partition coefficient K_d.

Finally, to check the quantitative aspect of the autoradiography, alpha counting has been compared to the HPGe gamma activity results. However, the HPGe gamma activity and the BeaQuant™ alpha counting needs to be standardized to the used volume of celestine samples, due to the fact that gamma emissions are detected from deeper in the volume of the sample compared to alpha emissions that are detected mainly from the surface of the sample. The section samples have been observed with SEM to evaluate the surface area of celestine grains in the section samples, while Monte Carlo simulations using Geant4 tools have allowed to calculate the maximum range of alpha particles from the celestine samples, which relates to the depth of alpha emissions determined by BeaQuant™.

The present paper aims to : 1) demonstrate that ^{226}Ra included into celestine grains/crystals is detectable from its alpha emission with BeaQuant™, 2) check the ability of the BeaQuant™ to quantify ^{226}Ra from its alpha emissions and 3) propose a method to study the ^{226}Ra distribution at the celestine grain/crystal scale (homogeneous or chemical zoning ?).

2. Materials and Methods

2.1. Sample preparation

2.1.1. Natural and artificial celestine samples doped with ^{226}Ra

Three samples of ^{226}Ra doped celestine were prepared in the CEA (French Atomic Energy Commission) following two protocols: samples S1 and S2 were obtained through coprecipitation experiments, whereas in sample S3, ^{226}Ra is incorporated in natural grains of celestine through recrystallisation experiment in the presence of ^{226}Ra spike. All the experiments were performed at 22°C temperature and normal air atmosphere. All solutions were prepared with deionized water (Milli-Q) and chemicals of ACS (American Chemical Society) reagent grade.

Precipitation of S1 and S2 celestine samples were obtained in batches by mixing equimolar (0.26 $mol.L^{-1}$) solutions of $SrCl_2,6H_2O$(>99.0% ALDRICH®) and Na_2SO_4(>99.0% ALDRICH®) in a final volume of 10 mL. ^{226}Ra (Isotope Products Laboratories (USA)) was spiked to the solution at two initial activities 763 ± 72 and 7633 ± 720 Bq, respectively, just before the addition of the Na_2SO_4 reactant. After coprecipitation (7 days), the supernatants were removed and filtered (0.2 µm) for ^{226}Ra analysis and solids were air dried and weighted (mass of 0.23 g for both S1 and S2).

S3 sample was obtained by gentle crushing of a natural centimetric-size celestine monocrystal, resulting 200 µm to 1 mm size grains (0.04 g). These grains were put in contact with Milli-Q water (4.92 mL). One week is necessary to be sure that equilibrium solid-solution is achieved, before adding the ^{226}Ra spike solution (i.e. 0.5g of a 2618 ± 240 $Bq.g^{-1}$ spike). After 25 weeks of contact with ^{226}Ra doped solution, supernatant was removed and filtered.

As the alpha-emitting ^{226}Ra decays also by emitting gamma with energy of 186.21 keV and intensity of 3.64% (Nudat), a high purity germanium detector (HPGe, ITECH-Instruments) has been used to analyze ^{226}Ra solutions (spike and supernatant). Solutions and standards were always measured in the same geometry (airtight plastic container of 50 mL) with completing to 50 mL the sample volume with deionized water. The InterWinner©6.0 software was used to calculate the activities taking into account the parent-daughter decay law. The detection limit of ^{226}Ra was estimated at 10 ± 5 Bq or 1.10^{-12} moles.

The gamma measurements confirm that around 98% of the ^{226}Ra initial activity is retained in the solid for the two coprecipitation experiments, leading to the final specific ^{226}Ra activities in solid estimated to 3251 and 32523 $Bq.g^{-1}$ for S1 and S2, respectively. For the recrystallization experiment, the final activity in the batch is measured to be 1052 Bq. The activity in the solid sample S3 is given by the mass balance relation between initial and final state and is estimated to be 6410 $Bq.g^{-1}$. Note that these HPGe specific activities correspond to ^{226}Ra contents in celestine about 89, 888 and 175 ppb of celestine for S1, S2 and S3 samples, respectively.

2.1.2. Processing section samples for autoradiography

The three dry and solid ^{226}Ra-$SrSO_4$ samples (powder form), have been mixed to an epoxy resin, to form thin tablets about 1 cm in diameter and about 1 mm thick (Figure 1). These tablets were then glued in a plastic holder to manufacture a parallelepiped sample (Figure 1). This support section is adapted to the sample holder of the autoradiographic device BeaQuant™ (see

section 2.3.2.). The whole mounted section sample, i.e. the powder/resin tablet embedded in the plastic support, has been polished to obtain the even/smooth surface (required for BeaQuant™) and to allow the ^{226}Ra-celestine grains to emerge at the sample surface. Although as limited as possible, an inevitable loss of celestine mass occurs thus between the two different form of samples, i.e. the initial solid form and the section form, due to the polishing operation. These preparatory works have turn out to be a long and arduous process what has taken almost four years.

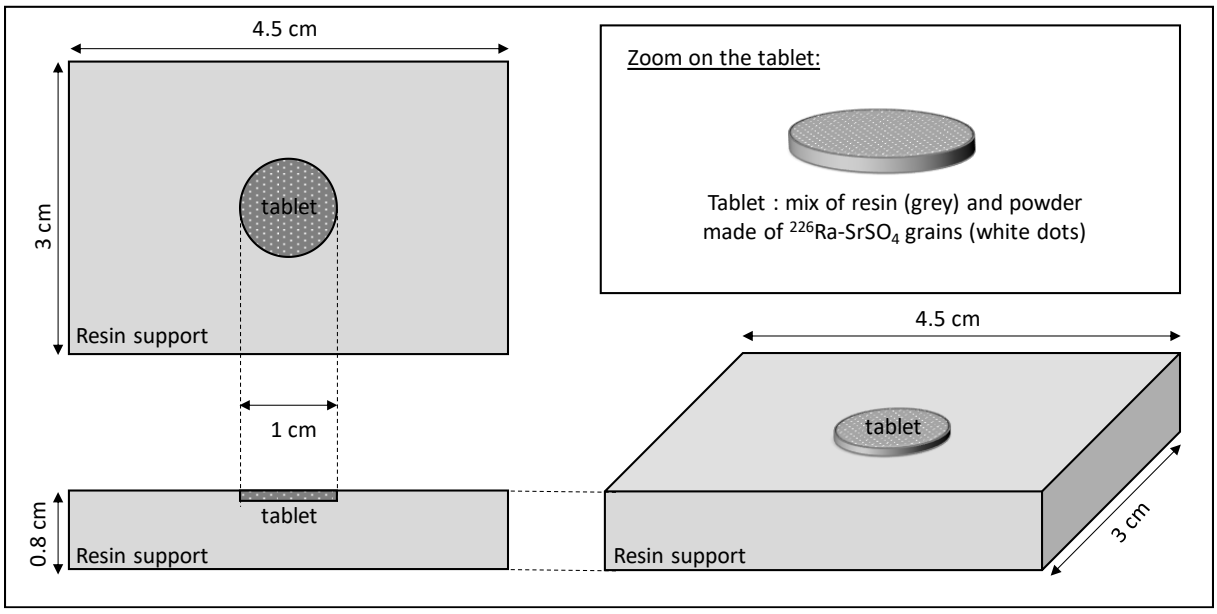

Figure 1. Geometry of the section samples.

2.2. Scanning Electron Microscope (SEM)

A JSM IT500 SEM has been used to observe and describe the celestine grains and their organization in the three studied section samples. The use of the backscattering electron mode (BSE) allows to discriminate the mineral grains and resin with the contrast of grey levels, since this observation mode is sensitive to the mean atomic number of the element in the mineral, while the secondary electron mode (SE) gives a relief picture.

The SEM was also equipped with an energy dispersive X-ray analyzer (EDS, silicon drift detector) which facilitated the identification of minerals thanks to their chemistry and their location with the construction of chemical maps. The analytical conditions included an acceleration voltage of 15 kV, a probe current of 1 nA and a working distance about 11 mm.

2.3. Radiation detectors

Table 1 summarizes the different radiation counting techniques used on the three samples and the used sample forms. Chemical micro-analysis of ^{226}Ra with EDS-SEM (or with WDS, i.e. wavelength dispersive spectroscopy) is indeed not effective here because of the too low content of ^{226}Ra in the samples.

Table 1. Radiation counting techniques used on the three samples S1, S2, S3 and the used sample form.

	S1	S2	S3
HPGe coaxial N-type γ spectrometry	Powder form	Powder form	Powder form
PIPS α spectrometry		Section form	
BeaQuant™	Section form	Section form	Section form

2.3.1. ^{226}Ra Decay Chain

^{226}Ra decay chain, which is part of the ^{238}U one, includes five alpha emitters with a 100 % intensity and four beta emitters with a 100% intensity too (Figure 2) (data from standards of the Laboratoire National Henri Becquerel). Only four of these radionuclides emit also gamma rays: ^{226}Ra, ^{214}Pb, ^{214}Bi and ^{210}Pb with intensity of 3.6, 64.5, 112.5 and 4.3 % respectively. Note that only gamma emissions with intensity > 0.1% have been considered. Auger and conversion electrons are also emitted by ^{226}Ra, ^{214}Pb and ^{210}Pb.

The half-life of ^{210}Pb (22.2 y) implies a delay of about 222 years before to reach the secular equilibrium for this whole decay chain. However, a secular equilibrium between ^{226}Ra and its first five daughters (^{222}Rn, ^{218}Po, ^{214}Pb, ^{214}Bi and ^{214}Po) is supposed after 40 days having regards to the half-life of ^{222}Rn (3.82 days). Alpha spectrometry measurement performed on the section sample S2 (see below), will be used to assess the equilibrium state, and the possible presence of ^{210}Po.

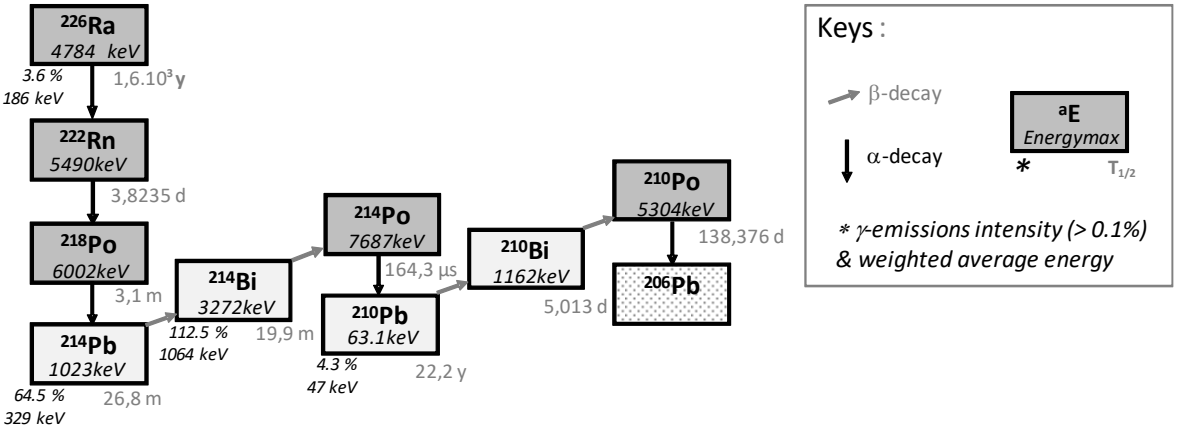

Figure 2. ^{226}Ra decay chain scheme. (data from standards of the Laboratoire National Henri Becquerel, France)

2.3.2. BeaQuant™ (autoradiographic device)

BeaQuant™ is a real-time digital autoradiographic device (Donnard, 2007; Donnard et al., 2009), based on a micro-pattern gaseous detector (MPGD) incorporating micromesh parallel ionization multiplier (PIM). Samples are deposited on the top of the gas chamber, the interest surface (i.e. the radioactive one) facing to the gas chamber, in such manner that radioactive particles emerging from a surface sample interact with gas (ionization) resulting in the creation of secondary electrons. Thanks to appropriate electric fields, secondary electrons are multiplied, drifted and localized on the segmented anode. Each initial particle triggering the acquisition electronic is thus reconstructed providing autoradiography image formation in real time.

BeaQuant™ allows to map and count the beta and alpha particles, while it is not affected by X or gamma rays. Both Auger electrons and conversion electrons can also trigger the acquisition electronic, in the same way as beta particles. However, a separation is possible between alpha and beta (or electron) particles, thanks to a threshold applied on the energy deposited in gas (far higher for alpha than for beta/electron).

High resolution images of the radioactivity are obtained, with a maximum reached for both alpha and ^{3}H detection (pixel of 20 µm). Due to the micromesh PIM structure, the sensitivity is about 8.10^{-4} cps.cm^{-2} (BeaQuant™ website), with a detection response linear of 5 orders of magnitude.

Samples analyzed with BeaQuant™ need to be perfectly flat: any unevenness can induce artefacts consisting of hot spots on the image/autoradiography. A customized sample holder called SM, designed for geological samples (i.e. with a section of 4.5 × 3 cm²), has been used

to measure surface alpha counting (in 2π sr) of the section samples. These counts are noted *C(B,α)* for Counting (BeaQuant™, alpha). The choice to focus exclusively on alpha emissions from ^{226}Ra decay is driven by the fact that alphas give a simple and well-defined signal, while the betas signal displays a broad emission energies distribution that is moreover polluted by numerous Auger and conversion electrons whose emission intensities are different from 100%. Moreover, an instrument detection efficiency for alpha particles from ^{238}U decay chain at secular equilibrium in natural rocks, has already been estimated ranging from 80 to 100% by Sardini et al. (2016).

2.3.3. The High Purity Germanium detector (γ-spectrometry)

γ-spectra have been acquired on the initial and final solutions of the coprecipitation and recrystallization experiments, allowing to deduce the activities of the three powder samples. The detector used is a N-type coaxial high purity germanium (HPGe) detector (ITECH-Instruments, French Atomic Energy Agency CEA) for which the detection limit is estimated at 10 ± 5 Bq for 186 keV energy. Corrections, including the system geometry, the Compton effect and the background measurement, have been applied using the InterWinner©6.0 software, which allows thus to assess the total activity of the ^{226}Ra decay chain, taking into account the parent-daughter decay law. That means that all the radiations (alpha, beta and gamma) are considered in the HPGe activities noted *A(HPGe)*. These activities will be used to assess the BeaQuant™ measurements.

2.3.4. Passivated Implanted Planar Silicon detector (α-spectrometry)

The alpha spectrum of the sample S2 presented in this work was obtained using a CANBERRA A450 Passivated Implanted Planar Silicon PIPS® detector (University of Helsinki, Department of Chemistry). This was performed in order to check the radioactive equilibrium state of the ^{226}Ra chain. The detector area is 450 mm^2 and intrinsic energy resolution (FWHM) of about 30 keV was achieved. The data acquisition and analysis were done with MAESTRO for Windows® Model A65–332 software. The energy calibration was performed with a reference sample containing ^{237}Np (E=4788 keV, I = 47%), ^{241}Am (E=5486 keV, I = 84.5%) and ^{244}Cm (E=5805 keV, I = 76.4%). The distance from the source to the detector was 6 mm. The number of energy channels was 1024. The acquisition time of the sample was 339615 s (almost 4 days). The AASI (Advanced alpha-spectrometric simulation) program (Siiskonen and Pollanen, 2005) has been used to correct the measurement from the instrument efficiency, from the system

geometry including the sample-detector distance and from the background measurements recorded in each used count chamber.

α-spectrum of sample S2 was used to evaluate the disequilibrium in the ^{226}Ra decay chain. The detector window is a 2.39 cm diameter, while ^{226}Ra-$SrSO_4$ crystals are concentrated in a tablet of 1 cm diameter: a mask window (1 cm diameter) has been used to restrict the counting zone to the real sample size. This mask is thus centered both to the tablet section and to the detector window. AASI (Advanced alpha-spectrometric simulation) program has also been used to perform a deconvolution of the α-spectrum in order to separate the various radionuclides proportions in a decay chain.

2.4. Geant4 simulations

The Geant4 Monte Carlo simulation toolkit (GEometry ANd Tracking 4) allows to simulate the transport of all kinds of particles through the matter (Agostinelli et al., 2003). Geant4.10.02.p02 version was used in this work to model the transport of alpha particles emitted from the ^{226}Ra decay chain into celestine. The alpha energy distributions have been extracted from standard provided by Laboratoire National Henri Becquerel, France.

Previous works have validated the implementing physics in Geant4 (Billon et al., 2019a ; Billon and Sardini, 2017), by successful comparisons of the maximum range R_{MAX} of alphas obtained with: 1- Geant4, 2- NIST database (National Institute of Standards and Technology) (Berger et al., 1999) and 3- Lapp-Andrews equation and Bragg-Kleeman rule (Lapp and Andrew, 1949; Bragg and Kleeman, 1905). Comparisons were performed using a data set including three different materials and alpha energies ranging from 4 to 8 MeV.

2.5. Comparative Methodology

The present paper aims to demonstrate the ability of BeaQuant™ to locate and quantify the ultratrace element ^{226}Ra. SEM observations allow to determine the celestine content of samples before performing a first qualitative comparison between SEM images and BeaQuant™ autoradiographs, and evaluate the ability to map ^{226}Ra on the sample scale. To go further, homogeneity or heterogeneity of the ^{226}Ra distribution can also be investigated on the celestine crystal/grain scale.

Then, alpha counting using BeaQuant™ is faced with the activity measured with HPGe detector. However, this quantitative comparison cannot be done straightforward, first because these two measurements have been performed on different forms and amounts of samples: total celestine grains powder for the HPGe measurements, and the polished sections for the BeaQuant™ acquisitions. Moreover, the volume of the ^{226}Ra doped celestine explored by these two techniques is non-equivalent due to the detection of different radiations. Even if HPGe detector gives a total activity of the whole ^{226}Ra decay chain (after numerous corrections), the determination is based on the detection of gamma rays, while BeaQuant™ is used to detect only alpha particles. The volume detected by BeaQuant™ alpha detector is not the same as the one by HPGe gamma detector, because gamma particles have long mean free path in matter compared to the short range of alpha particles (Billon et al., 2019b). Indeed, in a given sample volume, all alpha particles emitted deeper than their maximum range R_{MAX} are not able to reach the analyzed surface. As an example, 37% of 600 keV gamma rays are attenuated by 4 cm of concrete, while 100% of 4 MeV alphas are attenuated by 15 µm of concrete (Billon et al., 2019a; Billon et al., 2019b; Berger et al, 1999; Hubbel, 1969).

Thus, to be consistent, two quantitative comparison methods were performed:

1- Absolute comparison: Standardize the HPGe gamma spectrometry activities noted *A(HPGe)* to the volume considered for alpha counting with BeaQuant™. This standardized activity noted $A_{St}(HPGe)$ can be compared to the alpha counting of BeaQuant™ noted $C(B,\alpha)$.

2- Relative comparison: Standardize counts/activities to 1 g of celestine, i.e. compared the HPGe specific activity noted $A_{Sp}(HPGe)$ in Bq.g^{-1} to the specific alpha counting of BeaQuant™ noted $C_{Sp}(B,\alpha)$ in Cps.g^{-1}.

For both absolute and relative comparison methods, SEM images have been used to estimate the surface area occupied by celestine grains on the section samples noted S_{eG} (cm^2), through a simple threshold by boundaries in grey levels SEM-BSE images. Geant4 simulations have then been performed to calculate the maximum range R_{MAX} of alpha in celestine. R_{MAX} calculations have been performed with 10^5 particles, which is statistically enough.

S_{eG} and R_{MAX} allow to define the effective volume V_{eG} of celestine grains in the section samples, truly explored by surface alpha detector (equation 1a). However, sample thickness d (i.e. celestine grain size) can be lower than R_{MAX}, involving the consideration of a real volume V_r instead of V_{eG} (equation 1b).

$$V_{eG} = R_{MAX} \times S_{eG}, if\ R_{MAX} < d \quad (1a)$$

or

$$V_r = d \times S_{eG}, if\ R_{MAX} > d \quad (1b)$$

One of these volumes V_r and V_{eG} can then be used to standardize the HPGe gamma spectrometry activities (equations 2a and 2b), to apply the comparison method 1.

$$A_{St}(HPGe) = \frac{A(HPGe)}{M} \times \rho \times V_{eG} \quad (2a)$$

or

$$A_{St}(HPGe) = \frac{A(HPGe)}{M} \times \rho \times V_r \quad (2b)$$

Where $A_{St}(HPGe)$ is the HPGe activity standardized to the corresponding volume V_e or V_r (depending on values of R_{MAX} and d), M is the total mass of celestine powder for each sample (section 2.1.1.), and ρ is the celestine density (3.95 g.cm^{-3}).

These volumes can also be used to calculate the specific BeaQuant™ alpha counting of the section sample, noted $C_{Sp}(B,\alpha)$ (Bq.g^{-1}), to apply the comparison method 2 (equations 3a and 3b).

$$C_{Sp}(B,\alpha) = \frac{C(B,\alpha)}{V_{eG} \times \rho} \quad (3a)$$

or

$$C_{Sp}(B,\alpha) = \frac{C(B,\alpha)}{V_r \times \rho} \quad (3b)$$

In order to further the discussion around the quantitative comparisons, an alpha spectrum is also studied to describe the equilibrium state in the ^{226}Ra decay chain.

3. Results

3.1. ^{226}Ra chain equilibrium state

As the same ^{226}Ra tracer solution was used for the three batch experiments, leading to the three samples, only one sample (S2), was studied in PIPS alpha spectrometry. The alpha spectrum showed four distinct peaks around 4.79 MeV, 5.5 MeV, 6 MeV and 7.7 MeV corresponding respectively to ^{226}Ra, ^{222}Rn, ^{218}Po and ^{214}Po (Figure 3). A slight peak is suspected at 5.3 MeV

366 which could correspond to ^{210}Po, although the time needed to be at equilibrium with this
367 element is probably not reached (222 years) (Figure 2).
368 Peak intensities reflect the radionuclide activities measured on the surface sample. The peak
369 intensities are quite different from one radionuclide to the other, because of the different alpha
370 energies, and so the different maximum ranges in the sample. The most energetic the alphas
371 are, the higher is the number of alphas that reach the surface, giving highest peak intensity.
372 However, an AASI (Advanced alpha-spectrometric simulation) simulation, i.e. deconvolution
373 of the spectrum with each radionuclide contribution (Figure 3), has shown the four first alphas
374 are in secular equilibrium. That means for 1 alpha emitted from ^{226}Ra, the 3 following alpha
375 emitters ^{222}Rn, ^{218}Po and ^{214}Po produce each 1 alpha, while ^{210}Po produces 0.35 alpha according
376 to its peak intensity, giving a total of 4.35 alphas. Thanks to the determined ^{210}Po activity, the
377 age of the used ^{226}Ra spike solution is estimated to be ~14 years.

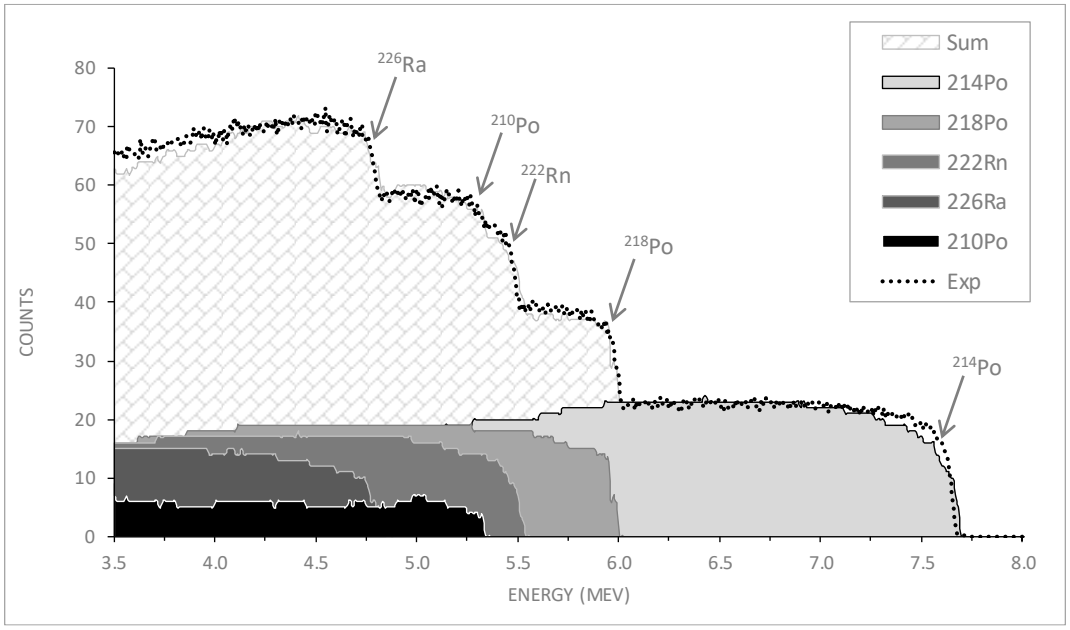

378

379 Figure 3. Alpha spectrum of the sample S2 (PIPS alpha spectrometer) (Exp: experimental,
380 dashed line) and AASI (Advanced alpha-spectrometric simulation) simulated curves for each
381 radionuclide and the sum of them.
382

383 **3.2. Section samples observations and descriptions**

384 Into the tablets of the section samples S1 and S2, celestine crystals are heterogeneously spread
385 into the resin (Figures 4A and 4C). In some areas, celestine crystals are associated with halite
386 observed mainly as cement between celestine forming aggregates (Figure 5A). In other sample
387 areas (always for both S1 and S2), celestine crystals/grains seems to be more homogeneously
388 dispersed into the resin (Figure 5B). Due to the heterogeneous grain arrangement and the

presence of halite, it was decided to work on several small regions of interest (ROIs) (Figure 4).

Sample S1 shows also large cubic crystals of halite (about 0.5 mm), which appear at the surface of the sample (in positive relief), probably in response to the atmospheric conditions (solubilization/recrystallization processes) (Figures 4A, 5A & 5B).

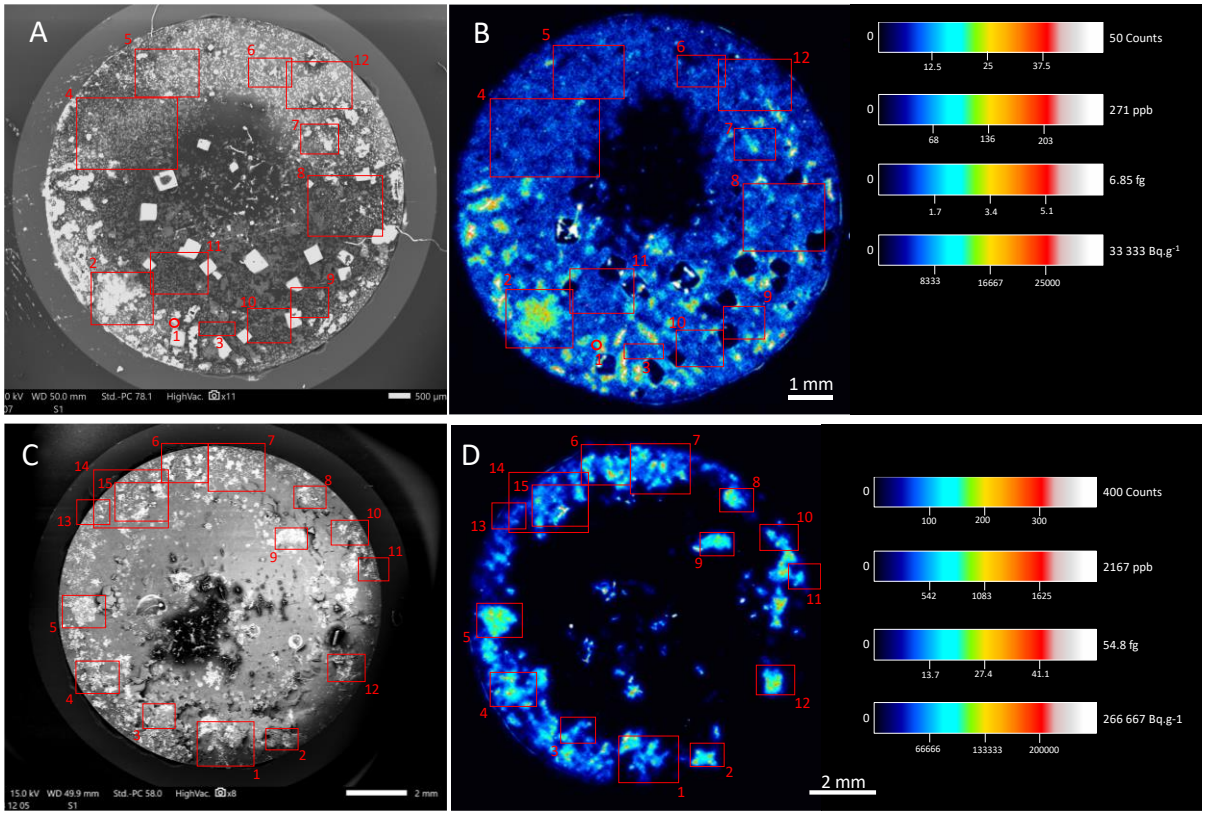

Figure 4. A & C- Overview of the tablet part of the section sample S1 and S2 respectively, using SEM-BSE imaging mode: the white grains are mainly celestine crystals (±halite), however the large cubic ones are halite. B & D- Alpha mappings (BeaQuant™) of respectively the S1 and S2 section samples. The counting scales have been recalculated to different units such as ^{226}Ra content (ppb in celestine), ^{226}Ra mass (fg) and ^{226}Ra specific activity (Bq.g^{-1} of celestine). These quantifications are performed for each pixel of the maps. ROIs are depicted in red in both SEM-BSE images and alpha mappings.

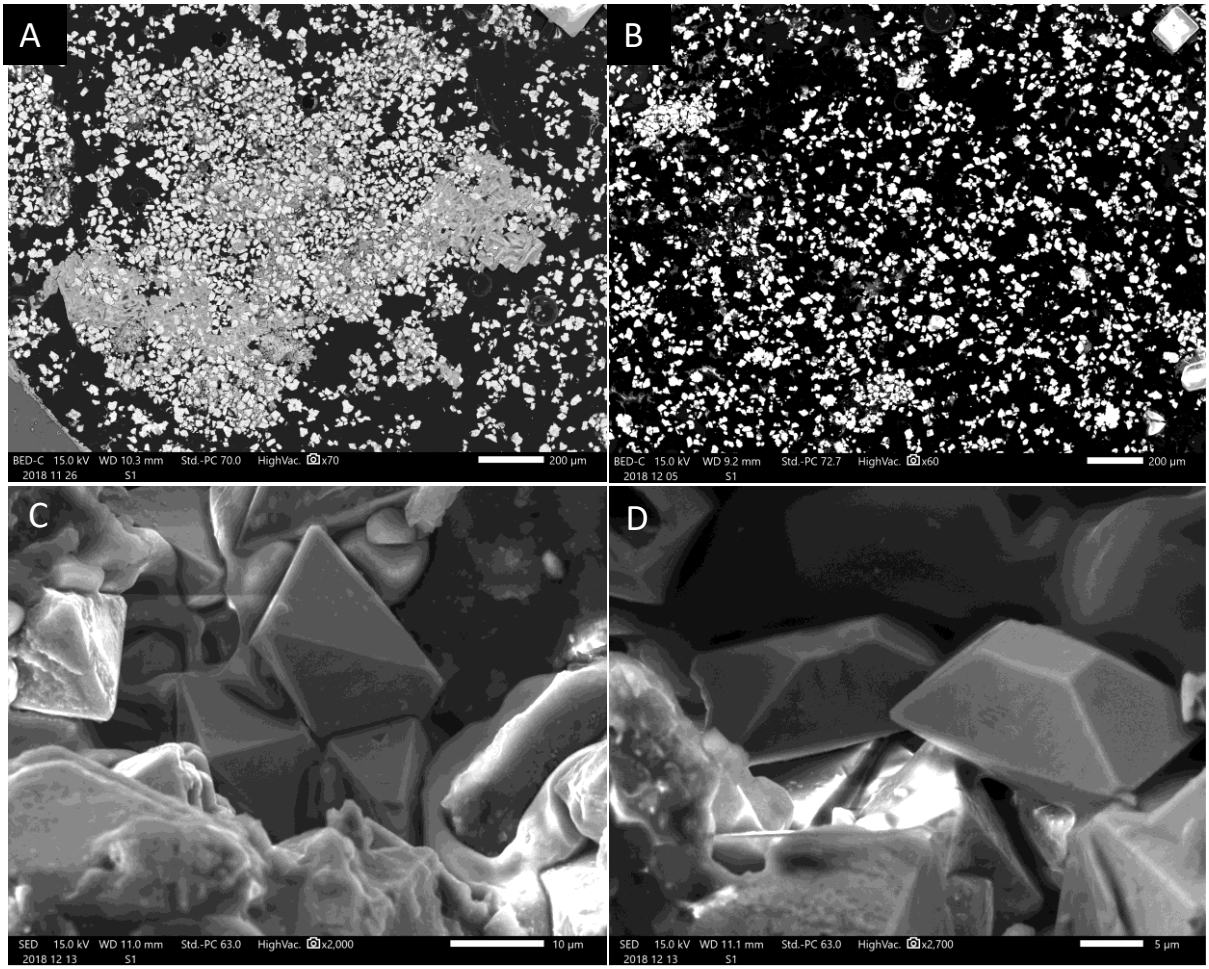

Figure 5. A- Zoom on the ROI 2 of the sample S1 using SEM-BSE imaging mode (see Figure 4A): celestine crystals (white) form a cluster partially cemented by halite (grey) in the bottom part of the cluster. Cubic crystals of halite are partially observable in the top right and bottom left corners. Resin appears in black. B- Zoom on the ROI 5 of the sample S1 using SEM-BSE imaging mode (see Figure 4A): celestine crystals (white) are quite homogeneously spread without halite cement. A cubic crystal of halite is present in the top right corner. Resin appears in black. C and D- Prismatic crystals of celestine in sample S2 using SEM-SE imaging mode.

SEM images acquired in secondary electron (SE) mode in some negative reliefs (generated by the grubbing up of some grains during the polishing operation) allowed to observe euhedral crystals of celestine under prismatic habit, with an average crystal size about 20±4 µm for S1 and about 25±4 µm for S2 (Figures 5C and 5D).

Sixty celestine grains ranging from 200 µm to 1 mm (average crystal size about 500 µm) were found from sample S3 (Figure 6A), which have been mostly damaged during their sampling on a celestine monocrystal; fracturation zones are thus visible on most of the grains of the S3 sample (Figure 6C).

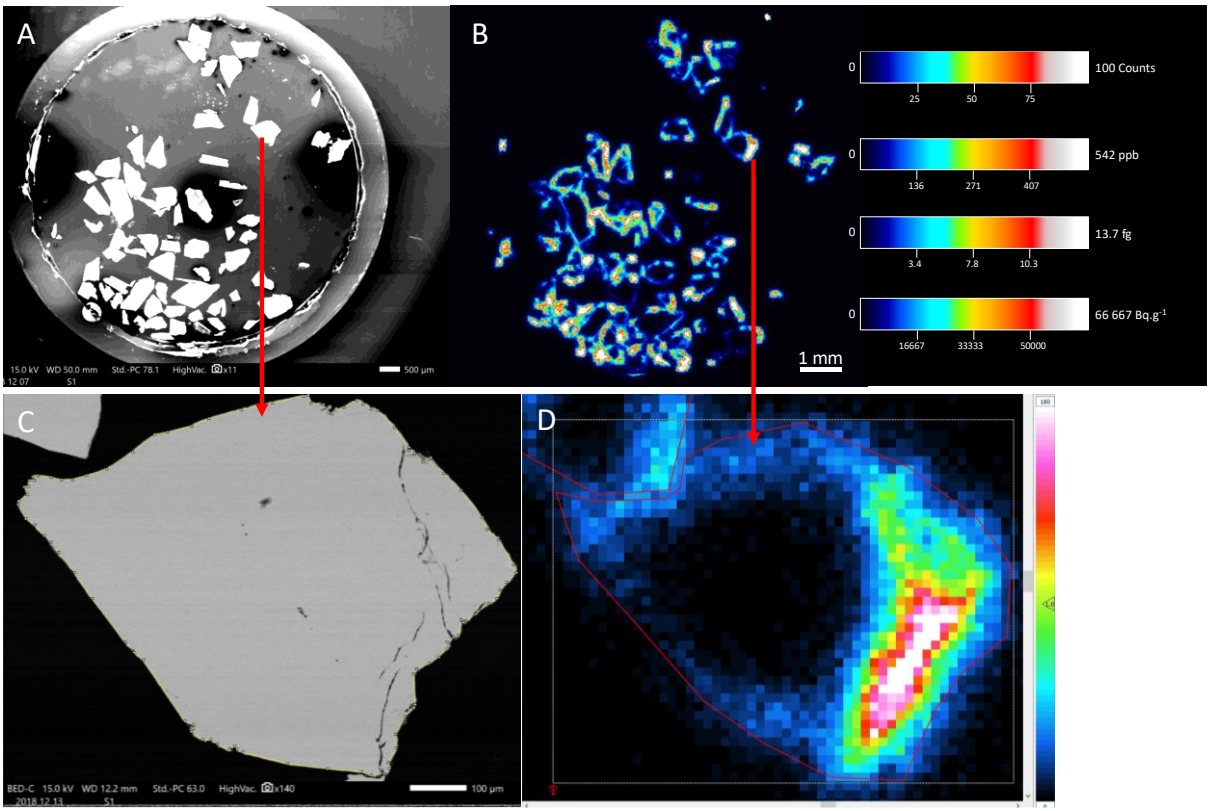

Figure 6. A- Overview of the tablet part of the section sample S3 using SEM-SE imaging mode: celestine grains are in white. B- Alpha mapping (BeaQuant™) of section sample S3. The counting scales have been recalculated in other units per pixel such as ^{226}Ra content (ppb in celestine), ^{226}Ra mass (fg) and ^{226}Ra specific activity (Bq.g^{-1}). C- SEM-BSE view of a fracturated celestine grain. D- Alpha mapping (BeaQuant™) of the grain displayed in Figure C. Color scale ranges from 0 (black) to 180 counts (white).

3.3. ^{226}Ra mappings on the sample scale : BeaQuant™ and SEM

Digital autoradiographs are maps of the alpha counts for a total acquisition time of 251 060 s (about 3 days). A good match is observable between celestine clusters on SEM images and high alpha counts areas on BeaQuant™ autoradiographs for samples S1 and S2, indicating that the location of ^{226}Ra-doped celestine can be performed with the alpha mapping of BeaQuant™. This match allowed easily to position the same ROIs on both SEM images and BeaQuant™

autoradiographs: 12 ROIs for sample S1 (Figures 4A and 4B) and 17 ROIs for sample S2 (15 ROIs + 2 sub-ROIs for ROI 7) (Figures 4C and 4D).

The large cubic crystals of halite occurring in S1 show also areas with high alpha counts, but they are counting artefacts due to the positive relief of these crystals (Figure 4B). As the pixel size (20 µm) used on the BeaQuant™ autoradiographs are in the same order of magnitude of the celestine crystal size (20-25 µm), it is not possible to go further in the qualitative evaluation for samples S1 and S2. However statistical calculations comparing crystal geometry and alpha counting are presented below (section 3.5), to study ^{226}Ra distribution into celestine, i.e. on a crystal scale.

The alpha map of S3 reveals that ^{226}Ra is located only on the edges of the celestine grains (Figures 6A and 6B). That is consistent with the dissolution/recrystallization process involved in the batch experiment. Indeed, only celestine grain surfaces were into contact with the ^{226}Ra spiked solution. Moreover, intra-granular fractures seem to be particularly rich in ^{226}Ra, allowing a deeper incorporation of ^{226}Ra thanks to the higher specific surface area created by the fractures (Figure 6C & 6D).

Some alpha counting profiles have been performed through grains displaying a regular halo (Figure 7): mean bulk width of the halos is about 240 µm while the mean value of the full width at half maximum (FWHM) is about 130 µm. These values do not reflect the recrystallisation thickness of ^{226}Ra-celestine, because they do not take into account the point spread function (PSF) of BeaQuant™ which deteriorates the signal, nor the fact that alpha particles travel laterally into celestine and resin from the edges of the celestine grains.

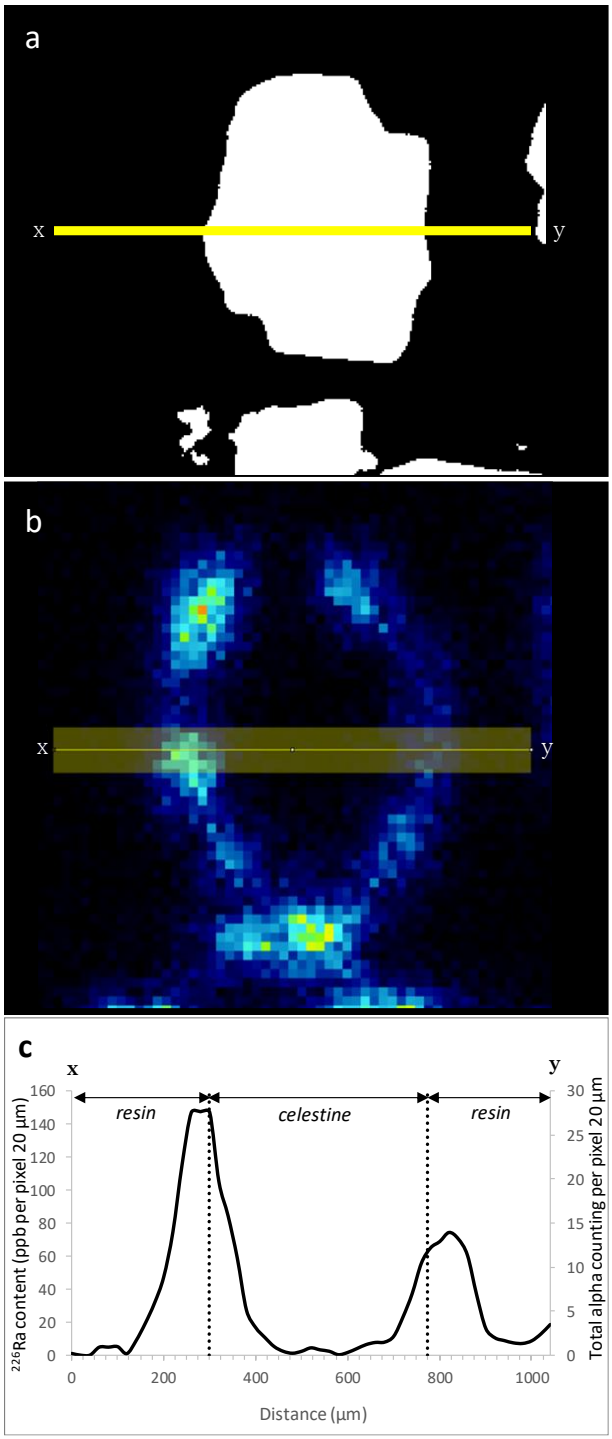

Figure 7. A- SEM-BSE binary image (i.e. after thresholding by boundary), celestine grain in white. B- Alpha map and location of the profile from x to y (100 µm width, 1040 µm long). C- ^{226}Ra content and total alpha counting along the profile from x to y.

3.4. ^{226}Ra quantification : BeaQuant™ Vs HPGe detector

In order to estimate the volumetric activity of ^{226}Ra-doped celestine from autoradiographs, it is necessary to know the maximal range (R_{MAX}) of alpha particles emitted from the ^{226}Ra decay

chain in the solid matrix, here celestine (Billon et al., 2019a). These ranges were calculated with Geant4 (Table 2). A weighted R_{MAX} has then been deduced from the weighted factor provided by the alpha-spectrometry (Figure 3). The weighted R_{MAX} of alpha particles (~22.3 µm) is comparable to the celestine mean crystal size in S1 and S2 (20-25 µm) and strongly lower than celestine mean grain size of S3 (500 µm). Then, a R_{MAX} value of 22.3 µm has been used to calculate the effective celestine grain volume V_{eG} (equations 1a) and to perform the standardization steps required for the quantitative comparison (equations 2a and 3a).

Table 2. Weighted average of the maximum range R_{MAX} (µm) of alpha particles emitted from the ^{226}Ra decay chain, calculated with Geant4 in celestine. Weight factors are deduced from α-spectrum (Figure 3).

Radionuclide	**^{226}Ra**	**^{222}Rn**	**^{218}Po**	**^{214}Po**	**^{210}Po**	**Weighted average of the R_{MAX} (µm)**
Maximum energy (keV)	**4784**	**5490**	**6002**	**7687**	**5304**	
Weighted factor (α-spectrometry)	**1**	**1**	**1**	**1**	**0.35**	
R_{MAX} (µm) in celestine	16.01	19.65	22.32	32.45	18.6	**22.3**

The effective celestine grain surfaces S_{eG} of the section samples (for each ROIs of S1 and S2, and the whole S3), deduced from a thresholding by boundary of BSE images are displayed in Appendices A, B and C for respectively S1, S2 and S3. Raw BeaQuant™ alpha counting is provided, as well as the specific alpha counting standardized to 1 g of celestine (celestine density is 3.95 g.cm^{-3}) (equation 3a). Finally, the HPGe activity has been standardized to the volume V_{eG} probed by alpha detector (equation 2a).

A quantitative comparison can be made by plotted BeaQuant™ alpha counting Vs HPGe standardized activity (Figure 8: plot of columns [5] and [7] from Appendices A, B and C). Good linear correlations are obtained for data from S1 and data from S2, with respective correlation coefficients about 0.988 and 0.996. Moreover, all the data of the three samples are aligned on the almost same slope ranging from 1.50 to 1.63 (1.3 for the single point of sample S3). This slope value indicates that BeaQuant™ alpha counting is 1.5 to 1.6 higher than total activity provided by the HPGe gamma spectrometry.

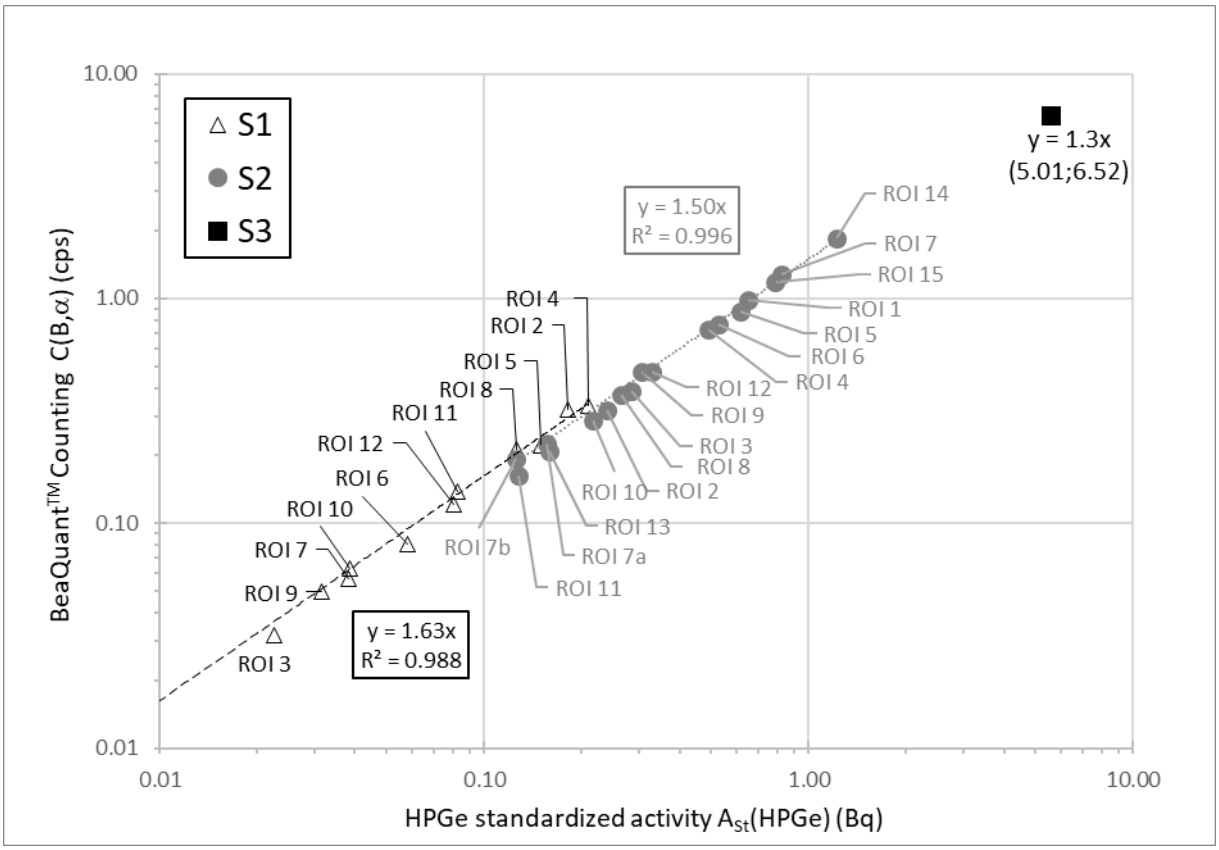

Figure 8. Absolute quantitative comparison for the three samples S1 (12 ROIs), S2 (17 ROIs) and S3 (1 single point) : BeaQuant™ alpha counting Vs HPGe activity standardized to the volume of celestine grain detected by alpha detector (V_{eG}).

Another way to perform a quantitative comparison consists to calculate the average of the BeaQuant™ specific alpha counting provided for each ROIs (Appendices A and B) (low Relative standard deviation about 5%), and to report the one for S3 (Appendix C) (Table 3). The ratio between BeaQuant™ specific counting and HPGe specific activity ranges between 1.2 to 1.6 (Table 3), which is close to the slope values found in the first comparison (Figure 8), always indicating a better detection efficiency for the BeaQuant™ device.

Table 3. Comparison of the mean specific alpha counting (average of the ROIs for samples S1 and S2), with the HPGe specific activity. RSD : relative standard deviation)

Samples		BeaQuant™ Specific α-counting $C_{Sp}(B,\alpha)$ (cps.g^{-1})	HPGe Specific Activity A_{Sp}(HPGe) (Bq.g^{-1})	Ratio BeaQuant™/HPGe
S1	Average ROIs	5075	3251	1.6
	Mean deviation	275		
	RSD (%)	6		
S2	Average ROIs	46808	32523	1.4
	Mean deviation	2126		
	RSD (%)	5		
S3	Value	7499	6410	1.2

Relative comparison can thus be made between the different samples activities/counts for a same detector (Table 4). Activity is 9.2 times higher in S2 than it is in S1 according BeaQuant™ alpha detector, while a factor 10 is reported for HPGe gamma detector. The S2/S3 activity factor is about 5.6 for BeaQuant™ and 5.1 for gamma detector, while 1.6 and 2 are obtained for the ratio S3/S1 with respectively alpha detector and HPGe detector. In general way, these factors are very close for the two detection technologies.

Table 4. Specific activity/counting factors between samples: BeaQuant™ Vs HPGe γ-spectrometry (calculated from specific counting/activity provided in Table 3).

Factors	BeaQuant™ Specific counting $C_{Sp}(B,\alpha)$ (cps.g^{-1}), after F_E correction	HPGe Specific Activity A_{Sp}(HPGe) (Bq.g^{-1})
$S2/_{S1}$	9.2	10.0
$S2/_{S3}$	5.6	5.1
$S3/_{S1}$	1.6	2.0

3.5. ^{226}Ra distribution on celestine crystal/grain scale

Alpha maps allow to locate ^{226}Ra into the sample, however what about ^{226}Ra distribution into celestine crystal/grain? That is an interesting question from a geochemistry point of view. Indeed, the incorporation of ^{226}Ra into the crystal lattice of celestine is allowed by the solid-solution between celestine and radium sulfate (Lestini et al., 2019). Two models can describe solid-solutions (partition coefficient calculation): first the heterogeneous model where equilibrium is governed by the solid-solution surface, the second the homogeneous model where all the solid-solution volume is at the equilibrium with the solution.

3.5.1. Coprecipitation experiment (S1 and S2)

For samples S1 and S2, individual crystals are not observable on the alpha map because their size (20-25 µm) are in the same order of magnitude than BeaQuant™ resolution (20 µm). It is thus not possible to visually study more precisely the ^{226}Ra distribution in the celestine crystal, through a concentration gradient.

However, to decide between the two distribution models previously presented (heterogeneous Versus homogeneous), it could be checked if the alpha counting is rather dependent on the celestine crystal volume or on the celestine crystal surface. As our sample sections imply to work in two dimensions, crystal surface becomes crystal perimeter and crystal volume becomes crystal surface. Note that the study is performed on crystals clusters (ROI) and not on individual crystals: as previously mentioned, crystal cannot be individualized on autoradiographs. Total crystal surface area and alpha counting have already been calculated in the ROIs. Total perimeter crystal has been obtained considering round particles with the diameter equal to the average between the vertical length and horizontal length.

Several theoretical relations between geometry and alpha counting can occur, according crystals shape and crystals size (Figure 9). To simplify the hypothetical presented cases, ^{226}Ra initial activity is considered to be the same for all the crystals, i.e. the same activity of the ^{226}Ra spike solution and the same percent of this activity retained in the crystal.

First case, crystals are non-uniform in shape (size non considered), inducing a non-correlation between total perimeter and total surface of crystals in a cluster (ROI) (Figure 9, Case 1). Thus, if ^{226}Ra distribution is homogeneous, alpha counting should be correlated to the surface crystals. And conversely, a correlation between alpha counting and perimeter involved an heterogenous distribution of ^{226}Ra.

Second case, crystals are uniform in shape but present different crystal sizes (Figure 9, Case 2): perimeter is correlated with surface, with as many linear regression lines as crystal sizes. Only one parameter, surface or perimeter, should be correlated with alpha counting according a unique slope for all the crystals.

Third case, crystals are uniform in both shape and size; a unique linear regression line is observable for the relation surface versus perimeter (Figure 9, case 3). No matter how the distribution of ^{226}Ra is, both perimeter and surface are correlated with alpha counting along a unique regression line, not allowing to decide between homogeneous and heterogeneous model.

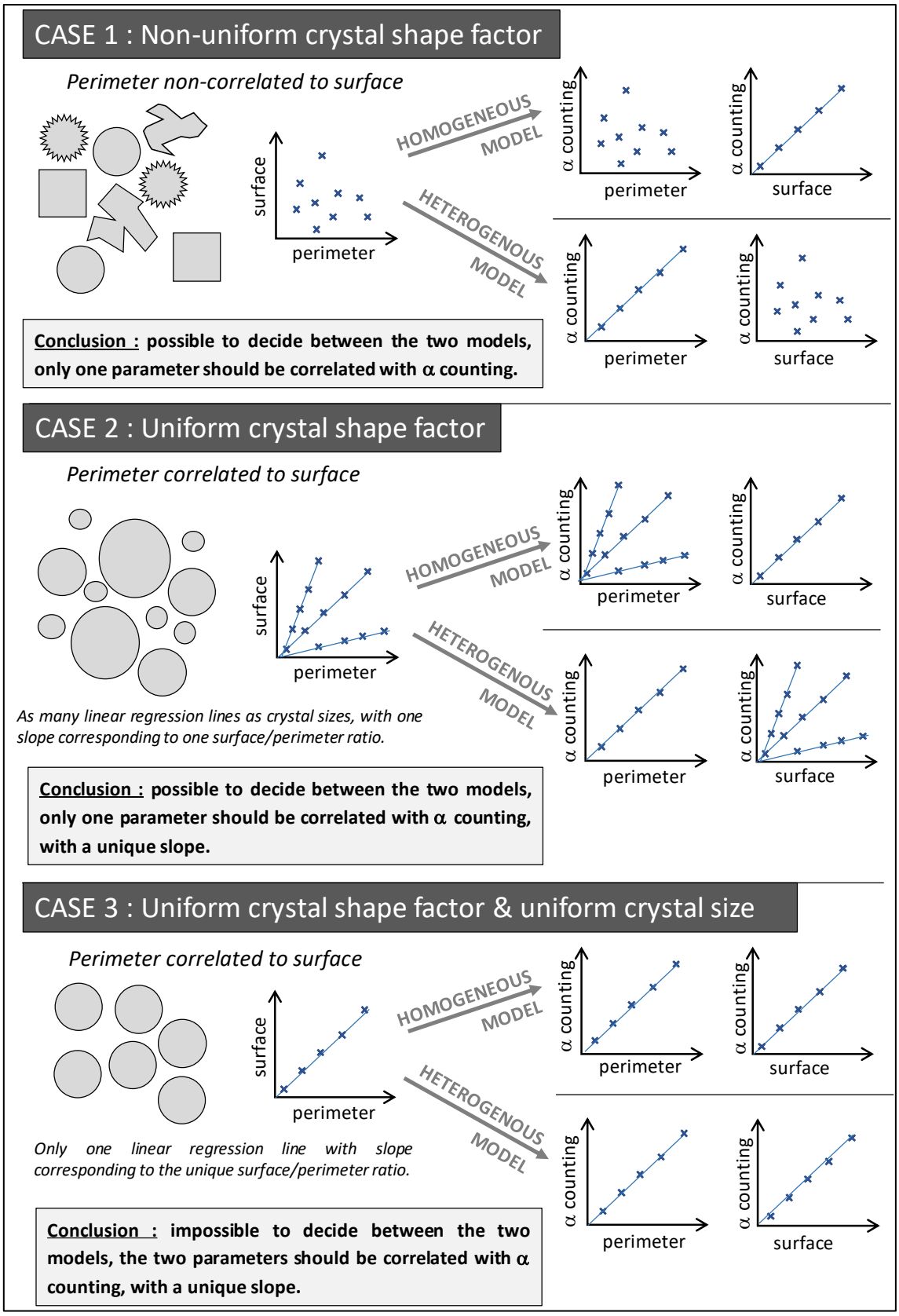

Figure 9: Three hypothetical cases of relations between crystal geometry and alpha counting into crystals clusters, to study ^{226}Ra distribution into crystal. Crystals are considered to originate from the same solution with the same ^{226}Ra initial activity.

The studied case, i.e. samples S1 and S2, shows a unique linear regression line between surface and perimeter for both samples, involving crystals are similar in shape and size (Figure 10 A). While two linear regression lines (one to each sample) appear for both surface/alpha counting and perimeter/alpha counting relations (Figure 10 B and C). As previously mentioned, initial activity of the ^{226}Ra spike solution was about ten times higher for sample S2 compared to sample S1. The factor between the slopes of the two sample is quite equal to the activity factor (Figure 10 B and C). Considering a same ^{226}Ra initial activity, the studied case corresponds to the case 3 presented in the Figure 9: it is not possible to decide between homogeneous and heterogeneous models.

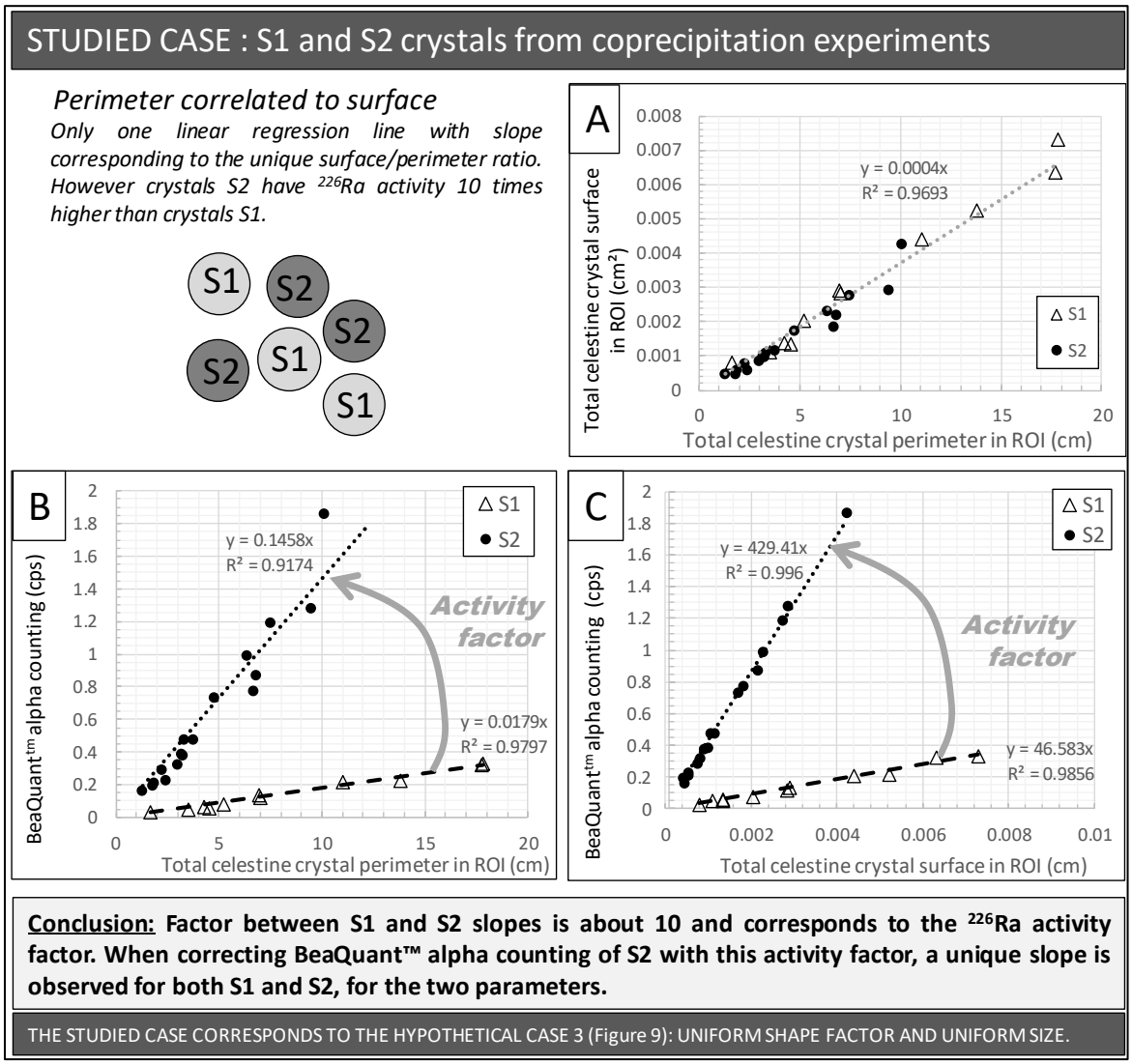

Figure 10: Relations between crystal geometry and alpha counting into crystals clusters of samples S1 and S2, to study ^{226}Ra distribution into crystal. ^{226}Ra initial activity is about 10 times higher for crystals S2, compared to crystals S1.

585 *3.5.2. Recrystallization experiment (S3)*

586 Visually, ^{226}Ra appears to be distributed on the edges of the celestine grains in sample S3, but
587 also in intergranular fracturation zones. Experimentation time has not been long enough to reach
588 an equilibrium between solution and solid: that is observed is ^{226}Ra penetration into celestine
589 grains. Concentration gradient should be studied on profiles, as presented in Figure 7, but PSF
590 of the alpha map and celestine edges effects are not yet defined, as previously mentioned.

591 In contrast to samples S1 and S2, S3 presents different grain sizes ranging from 200 to 1000
592 µm; this sample could be a good application of the method based on perimeter/surface and
593 allowing to decide between heterogeneous and homogeneous distribution model (Figure 9).
594 However, both perimeter/alpha counting and surface/alpha counting correlations are low and
595 not significant. Perimeter measurement is quite difficult with celestine grains in sample S3
596 which appears irregular and indented (Figure 6). Moreover, fracturation zones are contacts
597 between solution and solid which are not recorded for perimeter measurement. In other word,
598 perimeter is not really related to the grain contact with solution, explaining the non-correlation
599 between perimeter and alpha counting, which was however expected for this recrystallization
600 experiment.

601 ## 4.Discussion-conclusion

602 These results prove the effectiveness of the BeaQuant™ to locate and map the ^{226}Ra from its
603 alpha emissions, with a resolution about 20 µm directly related to the range of alpha in matter.
604 Better resolution about 1 µm can be reached with EDS or WDS (Wavelength-dispersive (X-
605 ray) spectroscopy) methods, however this resolution results from the electron-matter interaction
606 volume, which permits investigating a shallow sample depth (0.5 µm). Moreover, the detection
607 limit of these methods is in the ppm range: ^{226}Ra present concentrations far lower than ppm
608 (more commonly few ppb in natural occurrence), with activities higher than $Bq.g^{-1}$. Ultratrace
609 radionuclide, as ^{226}Ra, is definitely better detected by radiation detection.

610 To date, it is the first time that ultratrace ^{226}Ra, which is challenging to detect, is mapped on a
611 micrometer scale. The use of autoradiography is an obvious advantage for the detection of this
612 trace element. BeaQuant™ allows to count 20 to 25% of alpha particles emitted in a sample
613 thickness equal to the range of alpha (around 20 µm).

614

At the sample scale, S1 and S2 show a good match between celestine clusters on SEM images and high alpha counts area in autoradiography: BeaQuant™ can detect and locate ^{226}Ra included in celestine. However, on a smaller scale (within the crystal), ^{226}Ra distribution could not have been studied because of the crystal size which is too small to be visually individualized on alpha map (crystal size = alpha map resolution), and too similar between S1 and S2 to highlight relation between crystal surface, perimeter and alpha counting as demonstrated in Figure 10. An interesting prospect could be to perform new coprecipitation batch experiment with a much longer synthesis time, to produce larger crystal size of celestine. With two different populations of crystal size, the BeaQuant™ alpha counting would thus be studied according crystal surface, and according crystal perimeter to decide between homogeneous and heterogeneous distribution model for geochemistry calculation. Concentration gradient could also be studied from crystal edge to center part, if crystal size is sufficiently higher than BeaQuant™ resolution (20 µm).

The location of alphas in halo around the celestine grains of the sample S3 are consistent with the samples from recrystallization experiment, where only surface grains are affected by this process. This experiment was clearly not long enough to reach an equilibrium between solid and solution, however thickness of recrystallisation and concentration gradient could be determined providing to consider two effects: the point spread function (PSF) of BeaQuant™ and the grains side effect impacting alpha counting profiles at the interface between celestine and resin. Indeed, alpha range is longer in resin (lower density) than in celestine (higher density). A future study could be conducted to: i) determine the PSF of BeaQuant for the alpha emissions, ii) correct the experimental alpha counting profiles from the PSF, iii) simulate alpha profiles with Geant4, using various recrystallization thicknesses, and iv) compare corrected experimental and theorical profiles to identify the maximum recrystallization thickness of celestine grains. In addition, celestine grains in sample S3 are too irregular, indented and fractured to enable a comparison between grain geometry and ^{226}Ra distribution. New recrystallization experiments should be performed with synthetic celestine crystals (uniform shape, different sizes).

Finally, in terms of quantification, the BeaQuant™ allows to count alpha particles with a good linearity when compared to the activities provided by a HPGe gamma detector. Moreover, BeaQuant™ counting is higher than HPGe activity, whereas BeaQuant™ has been used to

count only alpha emissions from ^{226}Ra decay chain and HPGe activities are given for the whole emission of the ^{226}Ra decay chain daughter nuclides.

Since the ability of BeaQuant™ to quantify ^{226}Ra from the alpha emissions has been demonstrated, the maps of ^{226}Ra content can also been achieved (Figures 4B, 4D and 6B), through simple conversions from the alpha counting. Thus, ^{226}Ra content in celestine can be given as concentration (ppb), mass (fg) and of course as specific activity in celestine ($Bq.g^{-1}$). All these data, as well as the alpha counts, are calculated at the scale pixel of the autoradiographs (here 20 µm).

To conclude, the present work proves that ^{226}Ra quantitative mapping is easily achieved with alpha detection. The problem in the ^{226}Ra mapping occurs however when other alpha emitters cannot be neglected. This technology cannot discriminate between different alpha emitters. For instance, how to locate ^{226}Ra in uranium mine tailings, where ^{238}U and ^{234}U are still present in the material ? The approach considered by Angileri et al. (2018) combines both alpha and uranium mapping (alpha mapping using BeaQuant™ and U mapping using WDS microprobe analysis), to identify and locate equilibrium state in a section. More simply, qualitative comparison of U mapping and alpha mapping can also help to locate ^{226}Ra bearing minerals (mineral emitting alpha without U content). *Sensu stricto* ^{226}Ra mapping has not been however performed yet, regardless of U mapping. New developments are ongoing to obtain ^{226}Ra mapping for such natural materials.

The present study is the second one showing the ability of BeaQuant™ device to map and quantify alpha-emitting radionuclides (^{226}Ra this work, ^{238}U in Angileri et al. (2018), Sardini et al. (2016)): it can thus be assumed that all alpha-emitting radionuclides can be quantitatively mapped with this technology, opening up a wide range of applications in mining activities, nuclear waste storage and nuclear facilities decommissioning. Alpha mapping could be used to locate and identify alpha-emitter radionuclide retention sites in geo-materials as well to understand diffusion mechanisms using in-diffusion profiles (Siitari Kauppi et al., 1997). Being sensitive to betas and electrons, BeaQuant™ can also be used to locate and study the diffusion of beta-emitting radionuclides as well as Auger/conversion electrons emitters. Such works have already been performed on ^{133}Ba using Auger/conversion electron emission (Muuri et al., 2019).

Acknowledgements

We would like to thank Jean Charles Roussarie and Marc Brouand (ORANO Mining company) for the samples preparation, and the ORANO mining company for funding this work.

References

Agostinelli, S., Allison, J., Amako, K.A., Apostolakis, J., Araujo, H., Arce, P., Asai, M., Axen, D., Banerjee, S., Barrand, G., Behner, F., Bellagamba, L., Boudreau, J., Broglia, L., Brunengo, A., Burkhardt, H., Chauvie, S., Chuma, J., ... & Zschiesche, D. (2003). GEANT4 - a simulation toolkit. Nuclear Instruments and Methods in Physics Research Section A: Accelerators, Spectrometers, Detectors and Associated Equipment, 506, 250-303.

Angileri, A., Sardini, P., Donnard, J., Duval, S., Lefeuvre, H., Oger, T., Patrier, P., Rividi, N., Siitari-Kauppi, M., Toubon, H., & Descostes, M. (2018). Mapping 238U decay chain equilibrium state in thin sections of geo-materials by digital autoradiography and microprobe analysis. Applied Radiation and Isotopes, 140, 228-237.

Bacon, J.R., & Davidson, C.M., (2008). Is there a future for sequential chemical extraction ? Analyst 133, 25-46.

BeaQuant™ - Real-time autoradiography, http://www.ai4r.com/ Accessed 22 Sep 2018.

Berger, M.J., Coursey, J.S., & Zucker, M.A. (1999). ESTAR, PSTAR, and ASTAR: Computer programs for calculating stopping-power and range tables for electrons, protons, and helium ions (version 1.21). https://www.nist.gov/pml/stopping-power-range-tables-electrons-protons-and-helium-ions. Accessed 14 Jul 2018.

Billon, S., Sardini, P., Leblond, S., & Fichet, P. (2019a). From Bq cm− 3 to Bq cm− 2 (and conversely)—part 1: a useful conversion for autoradiography. Journal of Radioanalytical and Nuclear Chemistry, 320, 643-654.

Billon, S., Sardini, P., Leblond, S., & Fichet, P. (2019b). From Bq cm− 3 to Bq cm− 2 (and conversely)—part 2: useful dataset to apply the conversion to decommissioning operations. Journal of Radioanalytical and Nuclear Chemistry, 320, 699-709.

Billon, S., & Sardini, P. (2017). Présentation du code Geant4 et des tests de validation de la liste physique. Unpublished technical report for the French National Agency for Radioactive waste, University of Poitiers, France, 50 p.

Blanco, P., Tomé, F.V., & Lozano, J. (2004). Sequential extraction for radionuclide fractionation in soil samples: a comparative study. Low Level Radionuclide Measurement Techniques - ICRM, 61, 345–350.

Bordelet, G., Beaucaire, C., Descostes, M., & Phrommavanh, V. (2018). Chemical reactivity of natural peat towards U and Ra. Chemosphere 202, 651-660.

Bragg, W.H., & Kleeman, R. (1905). - XXXIX. On the α particles of radium, and their loss of range in passing through various atoms and molecules. The London, Edinburgh, and Dublin Philosophical Magazine and Journal of Science, 10(57), 318-340.

Déjeant, A., Galoisy, L., Roy, R., Calas, G., Boekhout, F., Phrommavanh, V., & Descostes, M. (2016). Evolution of uranium distribution and speciation in mill tailings, COMINAK Mine, Niger. Science of The Total Environment, 545, 340-352.

Déjeant, A., Bourva, L., Sia, R., Galoisy, L., Calas, G., Phrommavanh, V., & Descostes, M. (2014). Field analyses of 238U and 226Ra in two uranium mill tailings piles from Niger using portable HPGe detector. Journal of Environmental Radioactivity, 137, 105-112.

Donnard, J., Berny, R., Carduner, H., Leray, P., Morteau, E., Provence, M., Servagent, N., & Thers, D. (2009). The micro-pattern gas detector PIM : A multi-modality solution for novel investigations in functional imaging. Nuclear Instruments and Methods in Physics Research Section A: Accelerators, Spectrometers, Detectors and Associated Equipment, 610, 158-160.

Donnard, J. (2007). Étude et conception d'un imageur bêta à très haute résolution spatiale. PhD thesis of the university of Nantes, France, 204pp.

Hubbell, J.H. (1969). Photon Cross Sections, Attenuation Coefficients, and Energy Absorption Coefficients From 10 keV to 100 GeV. National Bureau of Standards.

Kalnins, C.A., Spooner, N.A., Clarke, M.J., & Ottaway, D. (2019). Alpha particle autoradiography for high spatial resolution mapping of radionuclides. Journal of environmental radioactivity, 197, 9-15.

Laboratoire National Henri Becquerel, Library for gamma and alpha emissions http://www.lnhb.fr/nuclear-data/module-lara/. Accessed 6 May 2018.

Lapp, R.E., & Andrew, H.L. (1949). Section 3 – Properties of Alpha, Beta, Gamma, X-rays and Neutrons: In Nuclear Radiation Physics, 562p. Prentice Hall Inc..

Leermakers, M., Phrommavanh, V., Drozdzak, J., Gao, Y., Nos, J., & Descostes, M. (2016). DGT as a useful monitoring tool for radionuclides and trace metals in environments impacted by uranium mining: case study of the Sagnes wetland in France. Chemosphere, 155, 142-151.

Lestini, L., Beaucaire, C., Vercouter, T., Ballini, M., & Descostes, M. (2019). Role of Trace Elements in the 226-Radium Incorporation in Sulfate Minerals (Gypsum and Celestite). ACS Earth and Space Chemistry, 3(2), 295-304.

Menozzi, D., Dosseto, A., & Kinsley, L.P.J. (2016). Assessing the effect of sequential extraction on the uranium-series isotopic composition of a basaltic weathering profile. Chemical Geology, 446, 126–137.

Muuri, E., Sorokina, T., Donnard, J., Billon, S., Helariutta, K., Koskinen, L., Martin, A., & Siitari-Kauppi, M. (2019). Electronic autoradiography of 133Ba particle emissions; diffusion profiles in granitic rocks. Applied Radiation and Isotopes, 149, 108-113.

Nudat. https://www.nndc.bnl.gov/nudat2/ Accessed 02 May 2019.

Phrommavanh, V., Leermakers, M., de Boissezon, H., Nos, J., Koko, M.B., & Descostes, M. (2013). Characterizing the transport of natural uranium and its decay product ^{226}Ra, downstream from former mines in France. Procedia Earth and Planetary Science **7**, 693-696.

Reinoso-Maset, E., & Ly, J. (2016). Study of uranium(VI) and radium(II) sorption at trace level on kaolinite using a multi-site ion exchange model. Journal of Environmental Radioactivity 157, 136-148.

Robin, V., Tertre, E., Beaucaire, C., Descostes, M., & Regnault, O. (2017). Experimental data and assessment of predictive modeling for radium ion exchange on swelling clay minerals with a tetrahedral charge. Applied Geochemistry 85, 1-9.

Sajih, M., Bryan, N.D., Vaughan, D.J., Descostes, M., Phrommavanh, V., Nos, J., & Morris, K. (2014). Adsorption of Radium and Barium on Goethite and Ferrihydrite: A kinetic and surface complexation modelling study. Geochimica et Cosmochimica Acta, 146, 150-163.

Sardini, P., Angileri, A., Descostes, M., Duval, S., Oger, T., Patrier, P., Rividi, N., Siitari-Kauppi, M., Toubon, H., & Donnard, J. (2016). Quantitative autoradiography of alpha particle emission in geo-materials using the Beaver™ system. Nuclear Instruments and Methods in Physics Research Section A: Accelerators, Spectrometers, Detectors and Associated Equipment, 833, 15-22.

Siiskonen, T., & Pöllänen, R. (2005). Advanced simulation code for alpha spectrometry. Nuclear Instruments and Methods in Physics Research Section A: Accelerators, Spectrometers, Detectors and Associated Equipment, 550(1-2), 425-434.

Siitari-Kauppi, M., Lindberg, A., Hellmuth, K. H., Timonen, J., Väätäinen, K., Hartikainen, J., & Hartikainen, K. (1997). The effect of microscale pore structure on matrix diffusion—a site-specific study on tonalite. Journal of contaminant hydrology, 26(1-4), 147-158.

Zhang, T., Gregory, K., Hammack, R.W., & Vidic, R. D. (2014). Coprecipitation of radium with barium and strontium sulfate and its impact on the fate of radium during treatment of produced water from unconventional gas extraction. Environmental Science & Technology, 48, 4596-4603.

Figures Captions

Figure 1. Geometry of the section samples.

Figure 2. ^{226}Ra decay chain scheme. (data from standards of the Laboratoire National Henri Becquerel, France)

Figure 3. Alpha spectrum of the sample S2 (PIPS alpha spectrometer) (Exp: experimental, dashed line) and AASI (Advanced alpha-spectrometric simulation) simulated curves for each radionuclide and the sum of them.

Figure 4. A & C- Overview of the tablet part of the section sample S1 and S2 respectively, using SEM-BSE imaging mode: the white grains are mainly celestine crystals (±halite), however the large cubic ones are halite. B & D- Alpha mappings (BeaQuant™) of respectively the S1 and S2 section samples. The counting scales have been recalculated to different units such as ^{226}Ra content (ppb in celestine), ^{226}Ra mass (fg) and ^{226}Ra specific activity (Bq.g^{-1} of celestine). These quantifications are performed for each pixel of the maps. ROIs are depicted in red in both SEM-BSE images and alpha mappings.

Figure 5. A- Zoom on the ROI 2 of the sample S1 using SEM-BSE imaging mode (see Figure 4A): celestine crystals (white) form a cluster partially cemented by halite (grey) in the bottom part of the cluster. Cubic crystals of halite are partially observable in the top right and bottom left corners. Resin appears in black. B- Zoom on the ROI 5 of the sample S1 using SEM-BSE imaging mode (see Figure 4A): celestine crystals (white) are quite homogeneously spread without halite cement. A cubic crystal of halite is present in the top right corner. Resin appears in black. C and D- Prismatic crystals of celestine in sample S2 using SEM-SE imaging mode.

Figure 6. A- Overview of the tablet part of the section sample S3 using SEM-SE imaging mode: celestine grains are in white. B- Alpha mapping (BeaQuant™) of section sample S3. The counting scales have been recalculated in other units per pixel such as ^{226}Ra content (ppb in celestine), ^{226}Ra mass (fg) and ^{226}Ra specific activity ($Bq.g^{-1}$). C- SEM-BSE view of a fracturated celestine grain. D- Alpha mapping (BeaQuant™) of the grain displayed in Figure C. Color scale ranges from 0 (black) to 180 counts (white).

Figure 7. A- SEM-BSE binary image (i.e. after thresholding by boundary), celestine grain in white. B- Alpha map and location of the profile from x to y (100 µm width, 1040 µm long). C- ^{226}Ra content and total alpha counting along the profile from x to y.

Figure 8. Absolute quantitative comparison for the three samples S1 (12 ROIs), S2 (17 ROIs) and S3 (1 single point) : BeaQuant™ alpha counting Vs HPGe activity standardized to the volume of celestine grain detected by alpha detector (V_{eG}).

Figure 9: Three hypothetical cases of relations between crystal geometry and alpha counting into crystals clusters, to study ^{226}Ra distribution into crystal. Crystals are considered to originate from the same solution with the same ^{226}Ra initial activity.

Figure 10: Relations between crystal geometry and alpha counting into crystals clusters of samples S1 and S2, to study ^{226}Ra distribution into crystal. ^{226}Ra initial activity is about 10 times higher for crystals S2, compared to crystals S1.

Appendices

Appendix A. Result data for the 12 ROIs of the sample section S1: Effective celestine grains data obtained on SEM images ([3] surface and [4] volume), BeaQuant™ alpha counting ([5] raw data and [6] standardized to 1 g of celestine), and [7] standardized HPGe activity.

		SEM data on celestine grains		BeaQuant™ measurements		HPGe γ-spectrometry
[1] ROIs	[2] total area (cm^2)	[3] Surface S_{eG} (cm^2)	[4] Volume V_{eG} (cm^3)	[5] α-counting C(B,α) (cps)	[6] Specific α-counting C_{Sp}(B,α) ($cps.g^{-1}$)	[7] Standardized activity (Bq)
ROI 1	4.08×10^{-04}	2.29×10^{-04}	5.10×10^{-07}	9.93×10^{-03}	4925	6.55×10^{-03}
ROI 2	2.46×10^{-02}	6.32×10^{-03}	1.41×10^{-05}	3.23×10^{-01}	5797	1.81×10^{-01}
ROI 3	3.30×10^{-03}	7.91×10^{-04}	1.76×10^{-06}	3.19×10^{-02}	4579	2.2610^{-02}
ROI 4	4.90×10^{-02}	7.29×10^{-03}	1.62×10^{-05}	3.33×10^{-01}	5185	2.09×10^{-01}
ROI 5	3.40×10^{-02}	5.22×10^{-03}	1.16×10^{-05}	2.22×10^{-01}	4835	1.49×10^{-01}
ROI 6	1.34×10^{-02}	2.03×10^{-03}	4.53×10^{-06}	8.12×10^{-02}	4537	5.82×10^{-02}
ROI 7	6.23×10^{-03}	1.34×10^{-03}	2.98×10^{-06}	5.67×10^{-02}	4815	3.83×10^{-02}
ROI 8	2.84×10^{-02}	4.39×10^{-03}	9.79×10^{-06}	2.12×10^{-01}	5490	1.26×10^{-01}
ROI 9	6.88×10^{-03}	1.11×10^{-03}	2.46×10^{-06}	4.94×10^{-02}	5073	3.16×10^{-02}
ROI 10	8.09×10^{-03}	1.34×10^{-03}	3.00×10^{-06}	6.31×10^{-02}	5325	3.85×10^{-02}
ROI 11	1.81×10^{-02}	2.89×10^{-03}	6.44×10^{-06}	1.39×10^{-01}	5461	8.27×10^{-02}
ROI 12	1.90×10^{-02}	2.83×10^{-03}	6.30×10^{-06}	1.21×10^{-01}	4877	8.10×10^{-02}

Appendix B. Result data for the 17 ROIs of the sample section S2: Effective celestine grains data obtained on SEM images ([3] surface and [4] volume), BeaQuant™ alpha counting ([5] raw data and [6] standardized to 1 g of celestine), and [7] standardized HPGe activity.

		SEM data on celestine grains		BeaQuant™ measurements		HPGe γ-spectrometry
[1] ROIs	[2] total area (cm^2)	[3] Surface S_{eG} (cm^2)	[4] Volume V_{eG} (cm^3)	[5] α-counting C(B,α) (cps)	[6] Specific α-counting $C_{Sp}(B,\alpha)$ ($cps.g^{-1}$)	[7] Standardized activity (Bq)
ROI 1	2.19×10^{-02}	2.28×10^{-03}	5.08×10^{-06}	9.88×10^{-01}	49276	6.52×10^{-01}
ROI 2	4.92×10^{-03}	8.32×10^{-04}	1.86×10^{-06}	3.19×10^{-01}	43562	2.38×10^{-01}
ROI 3	6.80×10^{-03}	9.92×10^{-04}	2.21×10^{-06}	3.86×10^{-01}	44194	2.84×10^{-01}
ROI 4	9.42×10^{-03}	1.72×10^{-03}	3.83×10^{-06}	7.28×10^{-01}	48045	4.93×10^{-01}
ROI 5	1.10×10^{-02}	2.16×10^{-03}	4.81×10^{-06}	8.70×10^{-01}	45780	6.18×10^{-01}
ROI 6	1.29×10^{-02}	1.84×10^{-03}	4.10×10^{-06}	7.70×10^{-01}	47581	5.26×10^{-01}
ROI 7	2.20×10^{-02}	2.87×10^{-03}	6.41×10^{-06}	$1.28\times10^{+00}$	50488	8.24×10^{-01}
ROI 7a	2.98×10^{-03}	5.45×10^{-04}	1.21×10^{-06}	2.25×10^{-01}	46936	1.56×10^{-01}
ROI 7b	2.73×10^{-03}	4.36×10^{-04}	9.71×10^{-06}	1.93×10^{-01}	50238	1.25×10^{-01}
ROI 8	5.22×10^{-03}	9.24×10^{-04}	2.06×10^{-06}	3.74×10^{-01}	45975	2.65×10^{-01}
ROI 9	6.25×10^{-03}	1.07×10^{-03}	2.38×10^{-06}	4.75×10^{-01}	50458	3.06×10^{-01}
ROI 10	8.20×10^{-03}	7.53×10^{-04}	1.68×10^{-06}	2.86×10^{-01}	43066	2.16×10^{-01}
ROI 11	5.40×10^{-03}	4.46×10^{-04}	9.94×10^{-07}	1.63×10^{-01}	41630	1.28×10^{-01}
ROI 12	8.19×10^{-03}	1.15×10^{-03}	2.55×10^{-06}	4.74×10^{-01}	46994	3.28×10^{-01}
ROI 13	5.06×10^{-03}	5.54×10^{-04}	1.24×10^{-06}	2.09×10^{-01}	42787	1.59×10^{-01}
ROI 14	3.99×10^{-02}	4.24×10^{-03}	9.46×10^{-06}	$1.86\times10^{+00}$	49804	$1.22\times10^{+00}$
ROI 15	1.85×10^{-02}	2.76×10^{-03}	6.15×10^{-06}	$1.19\times10^{+00}$	48923	7.90×10^{-01}

Appendix C. Result data for the sample section S3: Effective celestine grains data obtained on SEM images ([3] surface and [4] volume), BeaQuant™ alpha counting ([5] raw data and [6] standardized to 1 g of celestine), and [7] standardized HPGe activity.

		SEM data on celestine grains		BeaQuant™ measurements		HPGe γ-spectrometry
[1] ROIs	[2] total area (cm^2)	[3] Surface S_{eG} (cm^2)	[4] Volume V_{eG} (cm^3)	[5] α-counting C(B,α) (cps)	[6] Specific α-counting $C_{Sp}(B,\alpha)$ ($cps.g^{-1}$)	[7] Standardized activity (Bq)
S3	1.01×10^{-00}	9.87×10^{-02}	2.20×10^{-04}	6.52	7499	5.57